

1 Characterization of an INVS Model IV Neutron Counter for High 2 Precision (γ, n) Cross-Section Measurements

3 C.W. Arnold,* T.B. Clegg, H.J. Karwowski, G.C. Rich, and J.R. Tompkins

4 *Department of Physics and Astronomy,*

5 *University of North Carolina at Chapel Hill, Chapel Hill, NC 27599 and*

6 *Triangle Universities Nuclear Laboratory (TUNL), Durham, NC 27708[†]*

7 C.R. Howell

8 *Department of Physics, Duke University, Durham, NC 27708 and*

9 *Triangle Universities Nuclear Laboratory (TUNL), Durham, NC 27708[†]*

10 (Dated: October 24, 2018)

11 Abstract

12 A neutron counter designed for assay of radioactive materials has been adapted for beam exper-
13 iments at TUNL. The cylindrical geometry and 60% maximum efficiency make it well suited for
14 (γ, n) cross-section measurements near the neutron emission threshold. A high precision charac-
15 terization of the counter has been made using neutrons from several sources. Using a combination
16 of measurements and simulations, the absolute detection efficiency of the neutron counter was de-
17 termined to an accuracy of $\pm 3\%$ in the neutron energy range between 0.1 and 1 MeV. It is shown
18 that this efficiency characterization is generally valid for a wide range of targets.

19 PACS numbers: 29.40.Cs, 28.20.Gd, 07.05.Tp, 27.10.+h, 27.20.+n, 02.70.Uu

* cwarnold@physics.unc.edu

† <http://www.tunl.duke.edu>

20 I. INTRODUCTION:

21 The model IV inventory sample counter (INVS) developed at Los Alamos National Lab-
22 oratory [1] was designed for fast, non-destructive assay of radioactive materials. Specialized
23 inserts for the axial bore of this neutron counter have been made to adapt it for use as
24 the primary neutron detector for in-beam (γ, n) total cross section measurements. Develop-
25 ment and testing of this counter took place at TUNL using hadron beams in the tandem
26 laboratory and the γ -ray beam at the High Intensity Gamma-ray Source (HI γ S) [2].

27 Such measurements require detailed and accurate information about the energy-dependent
28 absolute neutron detection efficiency of the counter. Efficiency here is generally defined as

$$29 \quad \epsilon \equiv \frac{N_{detected}}{N_{emitted}}. \quad (1)$$

30 The efficiency measurements were made using four different sources, each with a precisely
31 known neutron emission rate. First, a ^{252}Cf source, calibrated by the National Institute
32 of Standards and Technology (NIST), generated a flux of neutrons known to $\pm 4.4\%$ [3].
33 Second, a coincidence experiment using the $^2\text{H}(d, n)^3\text{He}$ reaction provided a mono-energetic
34 source of 2.26 MeV neutrons with flux known to $\pm 10\%$, and gave insight into the thermal-
35 ization time of neutrons in the INVS. Third, an investigation of the $^7\text{Li}(p, n)^7\text{Be}$ reaction
36 produced <1 MeV neutron sources with fluxes known to $\pm 6.6\%$. Finally, the $^2\text{H}(\gamma, n)^1\text{H}$
37 reaction was used to produce tunable sources of monoenergetic neutrons ($0.1 \leq E_n \leq 1.0$
38 MeV) with fluxes known to $\pm 3\%$ accuracy. A comparison of all experimental data with
39 simulations demonstrates varying levels of agreement.

40 The following sections describe the detector geometry (Sect. II) followed by details for
41 each experimental setup (Sect. III) including discussions of backgrounds, calculations, mea-
42 surement uncertainties and results. Section IV contains a discussion of Monte Carlo simu-
43 lations used for comparison with experimental results. Finally, Sect. V offers a summary
44 of the results and a discussion of future applications of the INVS counter for cross-section
45 measurements.

46 II. DETECTOR DESCRIPTION:

47 The active detection elements in the INVS counter are 18 tubular proportional counters,
48 each containing 6 atm. of ^3He . The tubes are arranged in two concentric rings at radii 7.24

49 cm and 10.60 cm each containing nine equally spaced detectors (see Fig. 1). The detectors
50 are embedded in a cylindrical polyethylene body 46.2 cm long and 30.5 cm in diameter
51 which serves as a neutron moderator. The active length of the ^3He gas within the tubes
52 is 39.4 cm [1]. The detector body has an 8.9 cm diameter axial cavity designed to contain
53 the neutron source. Throughout this manuscript the term *longitudinal center* refers to the
54 center of the detector with respect to the length of the detector body, and is distinguished
55 from the term *axial center* which refers to the axis of the detector.

56 In experiments with beam, the irradiated target is the source of neutrons. During all but
57 one of the experiments described here, the neutron-emitting source was located inside the
58 detector cavity, usually near the longitudinal center. The cavity was partially filled with
59 additional neutron moderator (often graphite and/or polyethylene) to increase the detection
60 efficiency. The additional moderator was arranged so that the beam could pass through the
61 detector without intercepting moderator material.

62 Thermalization of the neutrons within the detector body increases the probability for
63 initiating the $^3\text{He}(n,p)^3\text{H}$ reaction within the embedded tubes. An energy of 763.7 keV,
64 shared between the outgoing proton and triton, is released from each reaction. Most of the
65 kinetic energy is lost to ionization of ^3He , which is detected as an electrical pulse on the
66 central electrode of each tube which is biased to +1780 V. A fixed threshold effectively dis-
67 criminates against low-pulse-height signals generated by γ -rays and electronic noise. Signals
68 above the threshold generate ~ 50 ns wide TTL pulses using on-board electronics. Onboard
69 signal-processing electronics within the detector produce three TTL logic output signals; the
70 inner ring (*I*); the outer ring (*O*); and the logical OR of the *I* and *O* pulses (*T*). Whenever
71 one or more tubes in the inner (outer) ring detect a neutron, a pulse is generated on the *I*
72 (*O*) output. For neutrons with energies less than about 2 MeV, the I/O ratio can provide a
73 reasonable determination of the mean of the energy distribution of the detected neutrons.

74 **III. EXPERIMENTS:**

75 In this section, the experimental setup and techniques used to measure the efficiency of
76 the counter are described, and the results of the each measurement are presented. Discussion
77 of the results will be presented in the next section. Four different sources of neutrons were
78 used to cover an energy range from about 0.1 to 10 MeV.

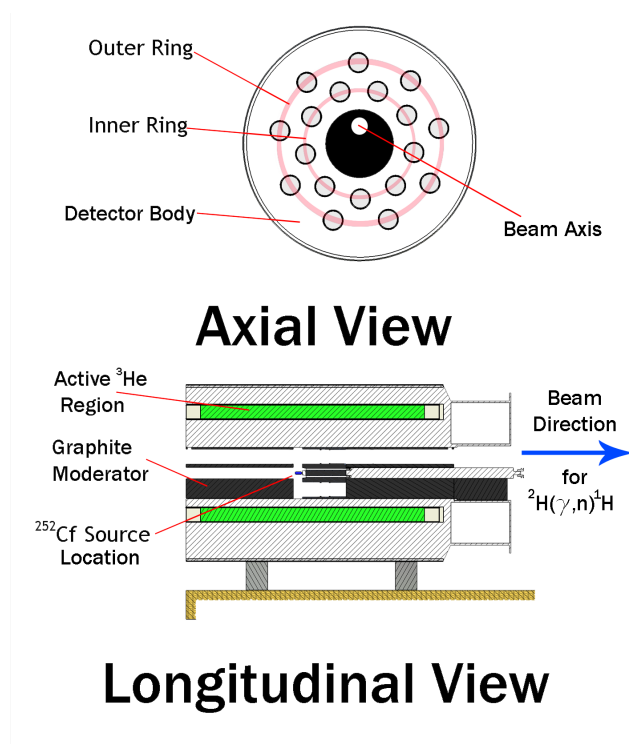


FIG. 1. (Color Online) Front and side cut-away cross-sectional views of the Model IV INVS counter described in the text. The arrangement of inter-cavity moderator corresponds to the experimental geometries either for the ^{252}Cf source measurement, or for the $^2\text{H}(\gamma, n)^1\text{H}$ experiment.

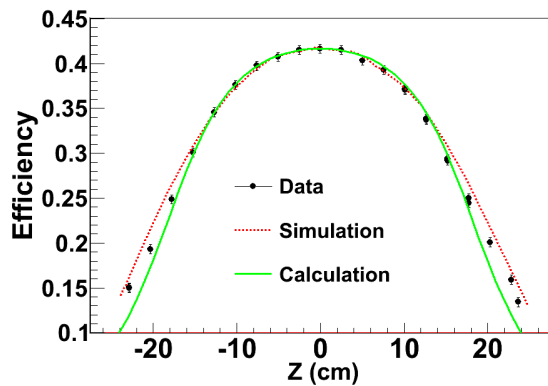


FIG. 2. (Color Online) Efficiency vs. Z-axis position for an open detector geometry.

79 **A. ^{252}Cf**

80 Californium-252 is a standard calibration source for neutron detectors. The effective half
 81 life of ^{252}Cf is 2.645 years and is due to alpha particle emission and spontaneous fission which

82 produces a neutron yield of 2.314×10^6 neutrons/s/ μg [4]. The energy spectrum of neutrons
 83 from ^{252}Cf is well known [5]. A calibrated ^{252}Cf source provides a single measurement of
 84 efficiency representing the response of the detector to a broad spectrum of neutron energies.

85 The ^{252}Cf source used consisted of 3.15 ng of active powdered material encapsulated
 86 within a small aluminum pellet. The source was suspended on the axis of the detector
 87 approximately 3.4 cm from longitudinal center. Graphite moderator filled most of the volume
 88 of the cavity. A table of neutron activity versus date was provided by NIST [3]. The
 89 experimentally determined efficiency for this configuration (shown in Fig. 1) was 40.5 ± 1.8
 90 %. The experimental I/O ratio was 1.516 ± 0.004 .

91 The dependence of the detection efficiency on the position of the source within the central
 92 cavity was determined by making measurements with the source placed at different positions
 93 within the central bore. Measurements on the central axis were made along the entire length
 94 of the detector. The detection efficiency has a maximum value at the longitudinal center and
 95 drops off smoothly as the source is moved in either direction away from the center along the
 96 detector axis. The shape of the position dependency is a purely geometric acceptance effect
 97 and can be approximated analytically for point sources with isotropic neutron emission. The
 98 measured detection efficiency as a function of the source position along the central axis of
 99 the counter is shown in Fig. 2 and in comparison to simulated and calculated efficiencies.

100 The relative efficiency is directly proportional to the angular acceptance of the counter
 101 as a function of z , which is given by the equation below for an isotropic point source of
 102 neutrons.

$$\begin{aligned}
 103 \quad \epsilon \propto d\Omega \approx & 4\pi \\
 104 \quad & -2\pi \times \left[\left(1 - \frac{L/2 - z}{\sqrt{(L/2 - z)^2 + r^2}} \right) \right. \\
 105 \quad & \left. + \left(1 - \frac{L/2 + z}{\sqrt{(L/2 + z)^2 + r^2}} \right) \right] \quad (2)
 \end{aligned}$$

106 Here, r is the radius of the opening at the end of the detector, L is the active length of
 107 the ^3He gas, and $z = 0$ at $L/2$. This function is maximum when $z = 0$. For an open cavity
 108 geometry, the change in the efficiency over the length of an 8-cm long sample, centered
 109 on the axis at the longitudinal center is approximately 1%. For a geometry like the one
 110 shown in Fig. 1 the changes in efficiency are negligibly small over a length of nearly 20 cm

111 centered on the longitudinal center. For sources located off its central axis, the detection
 112 efficiency changes by less than 0.5% . The radial dependence of the efficiency is also mostly
 113 a geometric acceptance effect.

114 B. ${}^2\text{H}(d, n){}^3\text{He}$

115 The ${}^2\text{H}(d, n){}^3\text{He}$ reaction was used to measure the efficiency for monoenergetic 2.26 MeV
 116 neutrons. The associated particle technique was used with the recoil ${}^3\text{He}$ nucleus detected
 117 in a siliFcon surface barrier detector inside an evacuated chamber. A schematic diagram of
 118 the experiment setup is shown in Fig. 3. The neutron counter was positioned so that its
 119 central axis coincided with the symmetry axis of the cone of neutrons associated with the
 120 ${}^3\text{He}$ particles detected in the silicon detector on the opposite side of the incident beam axis.
 121 The distance from the longitudinal center of the counter to the deuterium target was set so
 122 that the diameter of this neutron cone was smaller than the diameter of the central cavity
 123 through the detector. The energy of the incident deuteron beam and the detection angle of
 124 the silicon detector were set to produce 2.26-MeV neutrons emitted along the central axis
 125 of the counter. With this method the efficiency is computed as

$$126 \quad \epsilon = \frac{N_n}{N_{3He}} \quad (3)$$

127 where N_{3He} is the total number of detected ${}^3\text{He}$ -particles and N_n is the total number of
 128 neutrons detected in coincidence with the detected ${}^3\text{He}$ particles. This equation takes the
 129 detection efficiency of the silicon detector to be unity. The deuterium targets used in these
 130 measurements were $\sim 100\mu\text{g}/\text{cm}^2$ thick deuterated polyethylene (C_2D_4) evaporated onto a
 131 $10\mu\text{g}/\text{cm}^2$ thick carbon foil. The deuteron beam energy incident on the foil was 2.0 MeV,
 132 and the average beam current on the C_2D_4 foil was ~ 20 nA. The cross-sectional profile of
 133 the deuteron beam at the foil was circular with a diameter of approximately 0.5 cm. Each of
 134 the two silicon detectors (one in-plane and one out-of-plane) had a solid angle acceptance $d\Omega$
 135 $= \pi/60$ sr, and each was located at a scattering angle of $\theta_{lab} = 26.50^\circ$. Neutrons associated
 136 with detection of ${}^3\text{He}$ in the in-plane Si detector exited the target at $\theta_{lab} = 117.1^\circ$ along
 137 the central axis of the neutron counter. The rear half of the central cavity was plugged
 138 with polyethylene to scatter neutrons traveling through the central cavity into the body
 139 of the counter. The out-of-plane Si detector was used to measure the rate of accidental

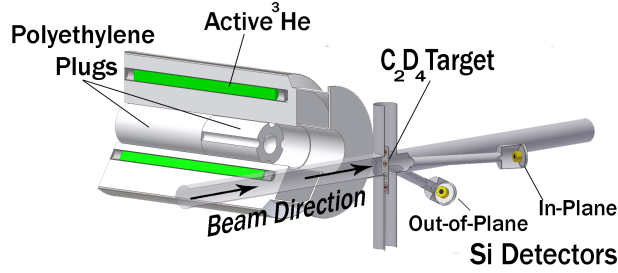


FIG. 3. (Color Online) Schematic diagram of the experimental setup for the efficiency measurements made using the ${}^2\text{H}(d, n){}^3\text{He}$ reaction at the tandem accelerator facility.

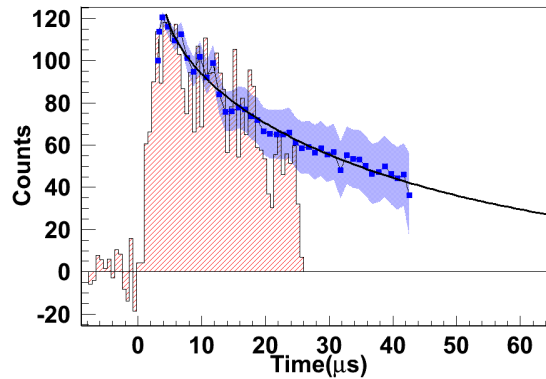


FIG. 4. (Color Online) The histogram is a background subtracted TAC spectrum from the ${}^2\text{H}(d, n){}^3\text{He}$ experiment. A simulated TAC spectrum (blue points) is shown in comparison to the experimental histogram. The solid curve is a fit to the simulated spectrum and predicts that most neutron detection occurs outside the $22.5 \mu\text{s}$ experimental window.

140 coincidences.

141 Efficiency and thermalization time were deduced simultaneously using a time-to-amplitude
 142 converter (TAC) which recorded the time between a charged particle detection in the silicon
 143 detector and a neutron detection in the INVS. A threshold setting effectively discriminated
 144 against deuteron elastic scattering events. The effective TAC range was $22.5 \mu\text{s}$. The
 145 TAC was calibrated using a pulser which started and stopped the TAC with known delay.
 146 Because the INVS is a thermalization counter, detection efficiency is time-dependent on a
 147 microsecond time-scale. A peak in the TAC spectrum at $\sim 3 \mu\text{s}$ suggests a source of delay
 148 exists caused by charge collection and signal processing in the INVS counter. This delay
 149 reduces the effective TAC range to $22.5 \mu\text{s}$ from $25.5 \mu\text{s}$, which is where the experimental

150 TAC spectrum ends. The present result for neutron detection efficiency over a 22.5 μs range
151 is $11.0 \pm 1.1\%$.

152 C. ${}^7\text{Li}(p, n){}^7\text{Be}$

153 The ${}^7\text{Li}(p, n){}^7\text{Be}$ reaction was used to measure the energy-dependent detection efficiency
154 over an energy range that overlaps with that covered by the ${}^2\text{H}(\gamma, n){}^1\text{H}$ source reaction below
155 about 0.7 MeV and to provide data for a neutron source with the intensity distribution
156 peaked at forward angles relative to the central detector axis [6, 7]. The cross section for
157 ${}^7\text{Li}(p, n){}^7\text{Be}$ reaction is large and has been accurately measured [8] making it a good neutron
158 source for calibrating the efficiency of detectors at low energies [9].

159 1. *Experimental Setup*

160 The experimental arrangement is shown in Fig. 5. The proton beam was tuned through
161 a double collimator set onto the LiF neutron production target. The cross-sectional profile
162 of the beam on target was circular with a diameter of 5 mm, and the average beam current
163 on target was 100 nA. The energies of the proton beams incident on the LiF target were
164 between 1.88 and 2.46 MeV. The neutron production target was comprised of 39.8 $\mu\text{g}/\text{cm}^2$
165 of LiF evaporated onto a 8.3 $\mu\text{g}/\text{cm}^2$ thick carbon backing. Targets were located on the axis
166 of the INVS counter inside an evacuated beam pipe at 14.2 cm from the longitudinal center.
167 The transmitted proton beam was collected in a voltage-suppressed Faraday cup at the end
168 of the beam pipe. A polyethylene plug was placed just beyond the end of the beam pipe to
169 increase detection efficiency. Backgrounds were measured by putting beam through both an
170 empty target ring identical to the one that supported the LiF target, and a target ring that
171 supported only a carbon backing. In total, beam-induced and environmental backgrounds
172 amounted to $\leq 0.1\%$ of real counts.

173 2. *Results*

174 The detection efficiency as a function of proton energy was calculated using

$$175 \epsilon(E_p) = \frac{N_n}{N_p N_t \sigma(E_p)} \quad (4)$$

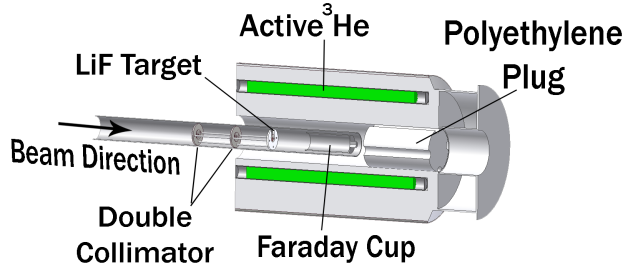


FIG. 5. (Color Online) Schematic diagram of the experimental setup for the efficiency measurements made using the $^7\text{Li}(p, n)^7\text{Be}$ reaction at the tandem accelerator facility.

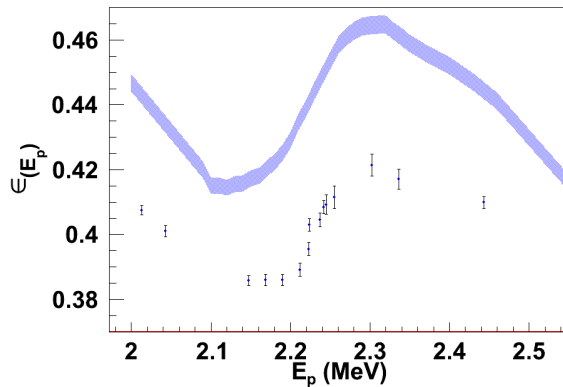


FIG. 6. (Color Online) For the $^7\text{Li}(p, n)^7\text{Be}$ reaction, a comparison of $\epsilon(E_p)$ as determined by experiment (points) and by simulation (band). Simulations, discussed in Sect. IV, reproduce the shape of the efficiency well.

176 where N_n is the total number of neutrons detected, N_p is the number of protons collected
 177 in the Faraday cup, N_t is the number of target nuclei per unit area, and $\sigma(E_p)$ is the total
 178 cross-section of the $^7\text{Li}(p, n)^7\text{Be}$ reaction at proton energy E_p .

179 The data (see Fig. 6) display a relative minimum in efficiency near $E_p = 2.13$ MeV followed
 180 by a relative maximum near $E_p = 2.32$ MeV. These shifts in efficiency coincide with rapid
 181 changes in the angular distribution of neutrons. Though statistical uncertainties were very
 182 small, systematic uncertainties for target thickness and cross-section contributed 3.5% and
 183 5%, respectively, resulting in an overall systematic uncertainty of 6.6%.

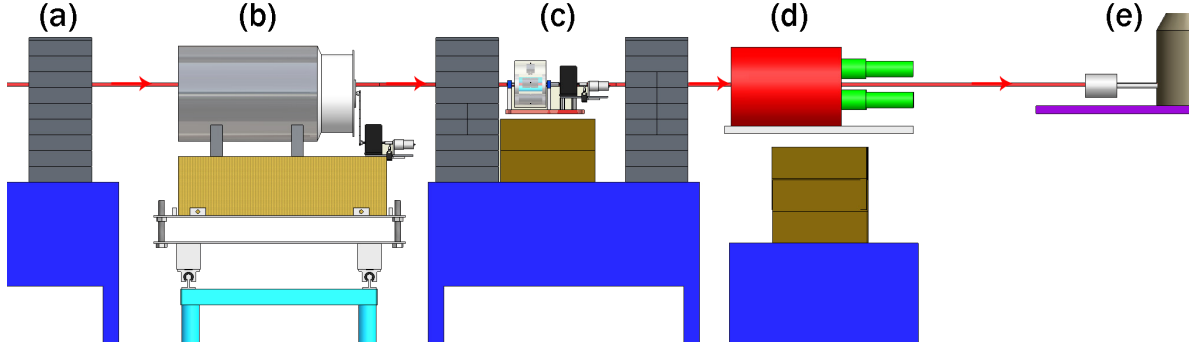


FIG. 7. (Color Online) Schematic of the experimental setup for measurements made using the ${}^2\text{H}(\gamma, n){}^1\text{H}$ reaction at the HI γ S facility. After collimation, the γ -ray beam passes through scintillation paddles (not shown) and into the target room. The 1.2 cm diameter γ -ray beam passes through the following elements: (a) "clean-up" collimator wall; (b) the D_2O target located near the longitudinal center of the neutron counter; (c) machined lead attenuators located between lead collimator walls; (d) a NaI detector; (e) an HPGe detector.

184 D. ${}^2\text{H}(\gamma, n){}^1\text{H}$

185 The ${}^2\text{H}(\gamma, n){}^1\text{H}$ measurement was unique among the experiments described here in that
 186 it produced nearly monoenergetic neutrons with very small flux uncertainties. Several ef-
 187 ficiency measurements were made that highlighted the energy-dependent response of the
 188 detector. A schematic of the experimental setup is shown in Fig 7.

189 1. *Experimental Setup*

190 The target consisted of approximately 3.2 g of 99.8% enriched D_2O sealed inside a thin-
 191 walled polyethylene tube that was 7.62 cm long. The target was located at longitudinal
 192 center, but 2.9 cm above the axial center, and occupied one of four 2.54 cm diameter az-
 193 imuthal holes in a rotatable graphite cylinder. The other holes were available for other
 194 targets. A graphite target and an empty hole were alternately rotated into the beam during
 195 experiments to determine beam-induced backgrounds. The samples were remotely rotated
 196 into position using a four-position Geneva mechanism which assured reproducible alignment
 197 on the γ -ray beam axis. Most of the data were collected for γ -ray beams with energies
 198 between 2.48 and 4.10 MeV.

199 Gamma-ray production by inverse-Compton scattering at HI γ S is well documented [2,
200 10, 11]. The γ -ray beams used in this experiment were collimated to 1.2 cm in diameter.
201 The size of the beam, and its alignment with the target was confirmed using a γ -ray beam
202 imaging system [12].

203 The γ -ray beam energy distribution was determined by a high purity germanium (HPGe)
204 detector located on the γ -ray beam axis. A radioactive ^{60}Co source, and naturally present
205 ^{40}K and ^{208}Tl provided energy calibration. The FWHM of the γ -ray beam as determined
206 by the HPGe was typically between 1 - 3%. A typical γ -ray spectrum is shown in Fig. 8.

207 Relative incident γ -ray flux was continuously monitored by three scintillating paddles
208 located upstream from the experimental setup. The absolute γ -ray fluxes were determined
209 by a cylindrical 25.4 cm \times 35.6 cm NaI detector located behind the active target, on the
210 γ -ray beam axis. For the γ -ray beam energies for which it was used, the NaI detector had
211 a total integrated efficiency of nearly 100%; In other words, nearly all γ -rays will interact
212 within the detector volume and deposit energy. A threshold setting which ignored signals
213 generated from γ -rays with energy less than ~ 0.6 MeV reduced the efficiency to $\sim 97\%$ for all
214 experimental γ -ray energies as determined by simulations. This threshold setting optimized
215 the ratio of total integrated signals to room background.

216 After passing through the target, the γ -ray flux was attenuated by machined lead atten-
217 uators to eliminate signal pile-up and dead-time effects. This allowed γ -ray flux on target
218 of $\geq 10^6 \gamma/\text{s}$, and flux at the face of the detector of $\leq 10^4 \gamma/\text{s}$. Determination of the absolute
219 beam flux from the signals measured in the NaI detector requires precise quantitative infor-
220 mation about the effective attenuation of the beam by the lead attenuators at each γ -ray
221 energy. The effective γ -ray attenuation, was determined for each attenuator, at several γ -ray
222 energies, using the scintillating paddle system for flux normalization.

223 *2. Background*

224 Two sources of neutron backgrounds existed in this experiment. One source is classified as
225 environmental backgrounds. These can be caused by either cosmic-ray neutron production
226 or natural radioactive sources in the vicinity of the INVS counter. These sources generated
227 0.2 count/s per ^3He tube for a total of 3.6 counts/s. The second background source arose
228 from γ -ray-beam-induced events. Gamma-rays that scatter from the target can deposit

229 enough energy to register a signal above the threshold setting. This type of background
 230 was measured by bombarding a graphite target with the γ -ray beam. Gamma-ray beam-
 231 induced backgrounds amounted to approximately 4.8 counts/ 10^6 γ -rays on target, which
 232 was typically $\leq 1\%$ of real counts from the heavy water target, and were taken into account
 233 in the data analysis.

234 3. Results

235 For the experimental setup used in these measurements the detection efficiency for neu-
 236 trons from γ -rays on a heavy water sample can be explicitly calculated from

$$237 \quad \epsilon_n(E_\gamma) = \frac{N_n \chi(E_\gamma) \epsilon_\gamma(E_\gamma)}{f N_\gamma N_t \sigma(E_\gamma)}, \quad (5)$$

238 where N_n is the number of neutrons detected, $\chi(E_\gamma)$ is the measured γ -ray attenuation by
 239 the lead attenuator at γ -ray energy E_γ , $\epsilon_\gamma(E_\gamma)$ is the efficiency of the NaI detector for
 240 γ -rays with energy E_γ , f is the thick target correction factor (described below), N_γ is the
 241 number of γ -rays detected, N_t is the number of target nuclei per unit area and $\sigma(E_\gamma)$ is the
 242 total cross-section of the ${}^2\text{H}(\gamma, n){}^1\text{H}$ reaction at E_γ [13]. The author of Ref. [13] calculated
 243 the ${}^2\text{H}(\gamma, n){}^1\text{H}$ total cross-sections with several widely-used N-N potential models, all of
 244 which were indistinguishable to within 1%, irrespective of the model used. In addition, this
 245 cross-section agrees with the world data which have uncertainties between 3 and 6% [14–17].

246

247 The f factor in Eqn. 5 accounts for the flux loss due to interactions with atomic electrons
 248 as the γ -rays propagate through the heavy water target. This factor is calculated as,

$$250 \quad f = \left(\frac{1}{e^{-\mu_w t}} \right) \left(\frac{(1 - e^{-\mu_w t})}{\mu_w t} \right), \quad (6)$$

251 using NIST attenuation coefficients for heavy water μ_w [18] and the mass thickness t of the
 252 target.

253 For photodisintegration of the deuteron E_γ and E_n are related, in units of MeV, by

$$254 \quad E_n = \frac{E_\gamma - 2.225}{2.001} \quad (7)$$

255 where -2.225 is the Q-value for the reaction, and the factor of 2.001 comes from energy
 256 sharing between the outgoing proton and neutron. Cross-sections for energies 2.48 MeV \leq
 257 $E_\gamma \leq 4.10$ MeV were used to ensure $\pm 1\%$ accuracy.

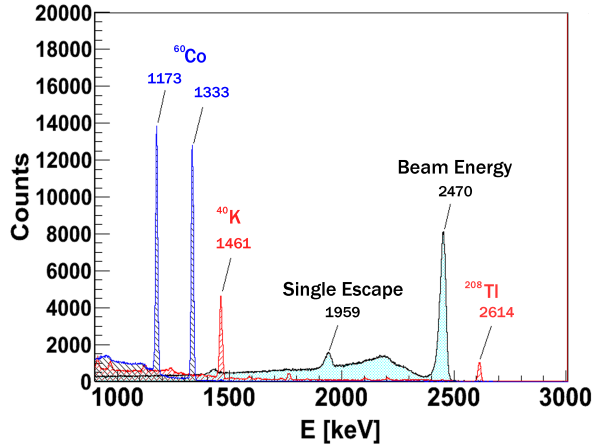


FIG. 8. (Color Online) A HPGe spectrum for 2.470 MeV γ -ray beam with $dE/E = 1\%$. Spectra of calibration γ -rays from ^{60}Co , ^{40}K , and ^{208}Tl are overlaid.

258 The total combined statistical uncertainty in the efficiency measurements made using
 259 neutrons from deuteron photodisintegration was $< 2\%$. The main source of statistical error
 260 was in the attenuation measurements of the lead absorbers. The statistical accuracy of
 261 these measurements was determined by the counts in the scintillator paddle system used
 262 for relative flux normalization between the absorbers. A minimum of $\pm 1\%$ statistical
 263 uncertainty was achieved for most energies. The statistical uncertainties in the γ -ray beam
 264 flux measurements and the neutron counting for the heavy water target were typically \leq
 265 0.5% .

266 The total systematic uncertainty was $< 3\%$ and was mainly due to three sources. The
 267 uncertainty in the deuteron photodisintegration cross section was kept to less than 1% by
 268 limiting the energy range of the measurements to $2.48 \text{ MeV} \leq E_\gamma \leq 4.14 \text{ MeV}$. Uncertainties
 269 in the target thickness and cross section contribute 0.5% and 1% respectively.

270 IV. DISCUSSION AND RESULTS:

271 A. Simulations:

272 The Monte-Carlo code MCNPX was used to simulate all particle interactions within the
 273 INVS counter for each experiment. For all simulations, material densities for the INVS
 274 counter were fixed, and standard thermal neutron capture cross-section libraries [19] were

275 used. Variable parameters in each simulation were:

- 276 1. the arrangement of materials inside the cavity;
- 277 2. the location of the neutron emitting source;
- 278 3. the energy and spatial distribution of neutrons.

279 Absolute detection efficiencies and I/O ratios were extracted from simulations for comparison
280 with each experiment where applicable.

281 1. ^{252}Cf

282 Efficiency measurements of ^{252}Cf were made during the course of the $^2\text{H}(\gamma, n)^1\text{H}$ exper-
283 iment. Consequently, the arrangement of materials inside the INVS cavity was identical
284 for both experiments. The energy distribution of neutrons produced by fissioning ^{252}Cf was
285 modeled as a Watt fission spectrum which has the form

$$286 \quad p(E) = C \exp(-E/a) \sinh(bE)^{1/2}, \quad (8)$$

287 where a and b are parameters given for ^{252}Cf [20].

288 The MCNPX-simulated efficiency of 39.2% agrees with the experimentally determined
289 efficiency of 40.5 ± 1.8 %. The simulated I/O ratio of 1.59 falls short of agreement with the
290 experimentally determined 1.516 ± 0.004 due to a 6% larger efficiency for measurement in
291 the outer ring (see Fig. 12). The source of this discrepancy is unclear.

292 2. $^2\text{H}(d, n)^3\text{He}$

293 The simulation of the measurements made with the $^2\text{H}(d, n)^3\text{He}$ reaction were made as
294 follows. A simulated beam of 2.26 MeV neutrons was emitted from inside an evacuated
295 volume, through an aluminum beam-pipe wall, directed toward the axial center of a set of
296 polyethylene plugs that filled most of the detector cavity (see Fig. 3). Because the experiment
297 only recorded counts in the neutron detector during a $22.5 \mu\text{s}$ wide time window after the
298 associated ^3He particle was detected, it was necessary to track the neutron detection time
299 in the simulations. Therefore, a time dependent model for detection of neutrons emitted
300 from the $^2\text{H}(d, n)^3\text{He}$ reaction was created to compare with experiment. In this model, only

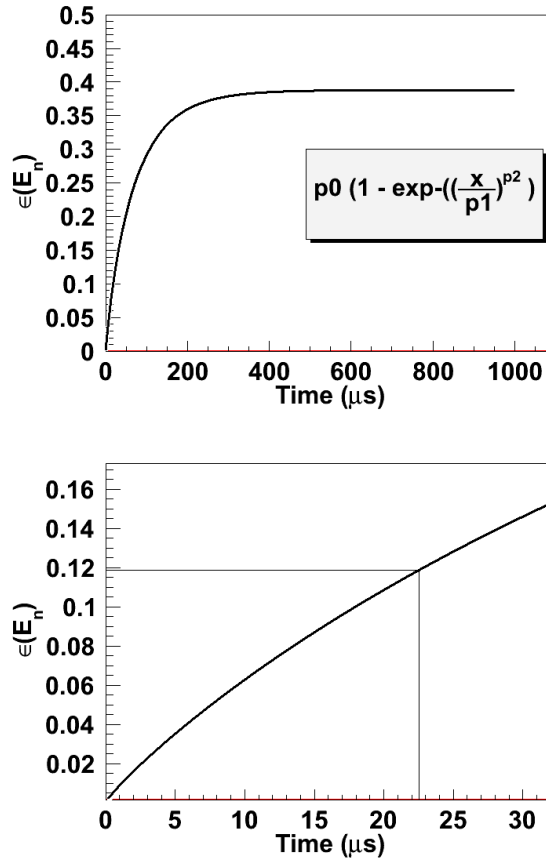


FIG. 9. (Color Online) (Top) A three parameter fit (solid line) describes the simulated efficiency of neutron detection as a function of time in the ${}^2\text{H}(d, n){}^3\text{He}$ experiment very well. (Bottom) The same plot expanded to show $t < 35 \mu\text{s}$. The vertical and horizontal lines identify the experimental window and expected efficiency.

301 neutrons detected before a user-defined time counted toward efficiency. A plot of efficiency
 302 vs. time was simulated for times between $t = 0$ and $t = 1000 \mu\text{s}$ (see Fig. 9). To produce a
 303 simulated TAC spectrum, a plot of the slope of $\epsilon(t)$ vs. time was generated for comparison
 304 with data (see Fig. 4).

305 The simulated total efficiency for neutrons collected between 0 and $22.5 \mu\text{s}$ is 11.9% in
 306 agreement with experiment. It is noteworthy, that simulations predict a relatively long time
 307 (nearly $500 \mu\text{s}$) before a maximum efficiency of 38.8% detection is realized for 2.26 MeV
 308 neutrons from the ${}^2\text{H}(d, n){}^3\text{He}$ reaction.

309 3. ${}^7\text{Li}(p, n){}^7\text{Be}$ and ${}^2\text{H}(\gamma, n){}^1\text{H}$

310 Simulations for the ${}^7\text{Li}(p, n){}^7\text{Be}$ and ${}^2\text{H}(\gamma, n){}^1\text{H}$ reactions were carried out in the following
311 way. First, the location of the source was set to match experimental conditions. For a single
312 simulation the source emitted monoenergetic neutrons only between angles θ and $\theta + d\theta$ with
313 constant emission over ϕ . After stepping through all of θ space, the process was repeated
314 for a new neutron energy.

315 Ultimately, a three-dimensional plot was constructed with neutron energy on the x-axis,
316 emission angle on the y-axis and detection efficiency on the z-axis (see Sect. V). After
317 choosing an incident particle energy, and inputting expected angular distributions for the
318 neutrons in the center-of-mass (CoM) frame, a second Monte Carlo process produced an
319 average efficiency for the given source conditions. This process was repeated for several
320 incident particle energies, and the result was a plot of simulated efficiency as a function of
322 incident particle energy.

323 For the ${}^7\text{Li}(p, n){}^7\text{Be}$ reaction, simulations reproduce very well the shapes of $\epsilon(E_p)$ for both
324 the inner and outer detector rings (see Fig. 11). Absolute detection efficiency for the outer
325 ring of detectors is in good agreement with experiment. A 13% systematic offset in absolute
326 efficiency is observed for the inner ring of detectors. Known systematic effects can account
327 for a maximum difference of 6.6%. The difficulty with this discrepancy is that it appears
328 to be of a systematic nature, while only affecting the inner ring of the INVS counter. A
329 missing thermal neutron sink in the model may explain the difference. An underestimated
330 amount of aluminum in the modeled beam pipe could have inadequately converted neutrons
331 to γ -rays, leaving an excess of thermal neutrons in the region of the inner ring of the INVS
332 counter.

333 For the ${}^2\text{H}(\gamma, n){}^1\text{H}$ experiment plots of $\epsilon(E_n)$ for the inner ring, the outer ring, and the
334 total show the data trends in good agreement with trends predicted by the simulation. The
335 data for total detection efficiency are systematically lower than simulation by about 5.9%.
336 Data for the inner and outer rings were systematically lower by 6.7% and 3.7% respectively.
337 These data provide a benchmark calibration for this INVS counter with regards to its use
338 in future (γ, n) experiments.

339 In the INVS counter a single detected neutron provides no information about the energy
340 of the neutron. However, the average neutron energy from an ensemble of detected neutrons

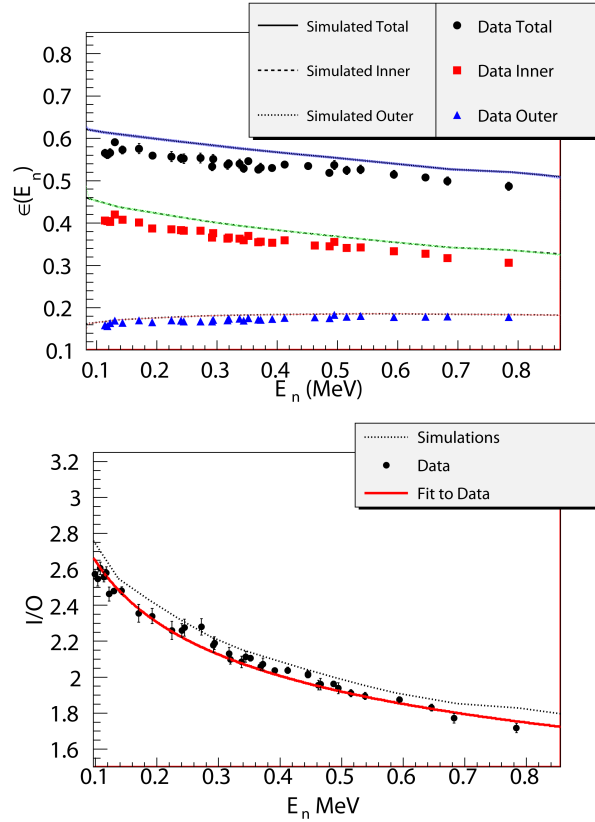


FIG. 10. (Color Online) The efficiency (a) and I/O ratio (b) are shown for neutrons detected during the ${}^2\text{H}(\gamma, n){}^1\text{H}$ experiment. Statistical error bars are smaller than the data points.

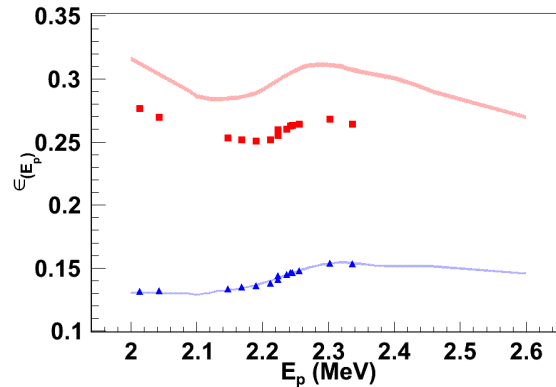


FIG. 11. (Color Online) Absolute efficiency for the inner ring (squares) and outer ring (triangles) of the detector during the ${}^7\text{Li}(p, n){}^7\text{Be}$ experiment. Statistical uncertainties are smaller than the data points. Simulations with uncertainties are shown as colored bands.

341 may be gleaned from the observed proportionality

$$342 \quad I/O \propto E_n^{-\frac{1}{5}}, \quad (9)$$

343 which is easily inverted. The ability to distinguish the signature I/O ratio for E_n from the
344 I/O ratio for $E_n + \Delta E_n$ becomes more difficult as E_n increases (see Fig. 10).

345 The method described above for evaluating detector efficiency is valid irrespective of the
346 target used. A deuteron target was chosen because of the precision with which the (γ, n)
347 cross section is known for this nucleus. Evaluating the efficiency this way established the
348 energy-dependent response of the detector for future users under certain conditions. The
349 efficiencies determined here are valid for any (γ, n) reaction measurement that satisfies the
350 following conditions: (a) the target location was fixed to match simulation; (b) the average
351 energy of the emitted neutrons is known; and (c) the CoM angular distribution is known. If
352 backgrounds are low, and the neutron energies are < 2.0 MeV, condition (b) may be relaxed,
353 because the neutron energy information may be obtained from the I/O ratio. For neutron
354 energies < 500 keV, condition (c) may also be relaxed because the response of the detector
355 is nearly constant with respect to angle of emission.

356 V. SUMMARY AND CONCLUSIONS:

357 The goal of this work was to characterize precisely the response of the highly efficient
358 INVS counter using multiple neutron sources with a focus on neutrons of energy < 1.0 MeV.
359 The attention to low energy neutrons was motivated by a need to generate high quality
360 (γ, n) cross-section data. Experiments were carried out and then simulated in detail for
361 comparison. In all simulations, special attention was given to assure accurate reproduction
362 of experimental conditions.

363 Figure 12 shows the ratio of experimentally determined efficiency to simulated efficiency
364 vs. average neutron energy for each experiment. Ratios have been determined for the inner
365 (I) and outer(O) rings separately, as well as for the total (T).

366 Neutrons from the ${}^2\text{H}(\gamma, n){}^1\text{H}$ reaction were emitted from within ± 4 cm from the longi-
367 tudinal center of the detector with a $\sin^2(\theta)$ distribution in the CoM frame which is hardly
368 changed when converted to the lab frame because of the relatively small momentum of
369 the incident γ -ray. The arrangement of moderating materials was approximatly symmet-

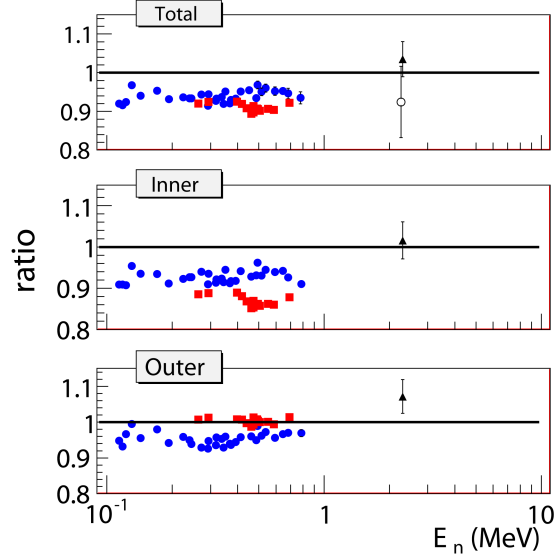


FIG. 12. (Color Online) Plot of the ratio of data to simulation for all experiments. Results for total ϵ_n , inner ring ϵ_n , and outer ring ϵ_n are shown. Blue filled circles are ${}^2\text{H}(\gamma, n){}^1\text{H}$ data; red squares are ${}^7\text{Li}(p, n){}^7\text{Be}$ data; black triangles are ${}^{252}\text{Cf}$ data; open circles are ${}^2\text{H}(d, n){}^3\text{He}$ data.

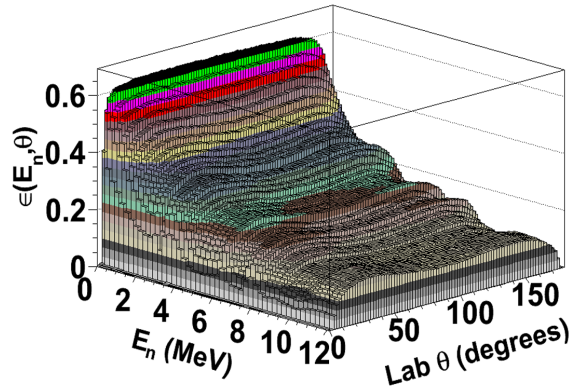


FIG. 13. A three-dimensional plot of efficiency vs E_n and θ_{lab} using a likely arrangement of moderator for (γ, n) experiments at HI γ S. The simulated neutron-emitting target was at the axial and longitudinal center of the detector. The simulated geometry filled the detector cavity with graphite except for a 2.54 cm diameter hole for the target and γ -ray beam.

370 ric. Under these conditions, simulations reproduce measurements to within a normalization
 371 of -6.7% (*I*), -3.7% (*O*), and -5.9% (*T*). These differences are likely the result of effec-
 372 tive threshold settings on the signals from the detector tubes. This feature of the effective

373 threshold settings was not included in the simulations.

374 Neutrons from the ${}^7\text{Li}(p, n){}^7\text{Be}$ reaction were emitted far from the longitudinal center
375 of the detector with a Legendre polynomial series distribution in the CoM frame which is
376 significantly changed when converted to the lab frame because of the relatively large mo-
377 mentum of the incident proton. The arrangement of moderating materials was asymmetric
378 - biased to achieve higher detection efficiency for neutrons emitted near θ_{lab} close to zero.
379 Under these conditions, absolute detection in O is reproduced very well by simulations; how-
380 ever, absolute detection in I is systematically 13% smaller than predicted by simulations,
381 resulting in a nearly 10% systematic difference in T .

382 The difference in the level of agreement between simulations and experiment for I and O
383 for the ${}^7\text{Li}(p, n){}^7\text{Be}$ reaction is intriguing. The most likely explanation is that the amount of
384 aluminum in the intervening beam pipe was underestimated in the simulations which caused
385 an excess of thermal neutrons in the vicinity of I .

386 The systematic differences between experiment and simulation for I , O and T for the
387 ${}^2\text{H}(\gamma, n){}^1\text{H}$ measurement confirmed the need for a well known, tunable, monoenergetic neu-
388 tron source. Reliance on simulations alone would have introduced systematic errors in future
389 (γ, n) measurements on the order of 6%. Using the cross-section of Ref. [13] as a 1% standard
390 provided tunable monoenergetic neutron sources with fluxes known to $\pm 3\%$. The method
391 for simulating absolute detection efficiencies for the ${}^2\text{H}(\gamma, n){}^1\text{H}$ reaction was not significantly
392 influenced by the choice of target material. Thus, using the same techniques, other (γ, n)
393 cross-sections may be measured with very high accuracy.

394 For the purpose of planning future (γ, n) experiments at HI γ S which seek to use the INVS
395 counter, simulations have been prepared for three likely experimental setups. An analysis
396 program takes as input the geometry, the desired (γ, n) reaction, the incident particle energy,
397 and the CoM angular distribution of the outgoing neutrons and gives as output the expected
398 detection efficiency and I/O ratio. The capabilities offered by the combination of the HI γ S
399 facility and this precisely characterized INVS counter make possible absolute photonuclear
400 cross-section measurements with high precision.

ACKNOWLEDGMENTS

Work supported in part by USDOE Office of Nuclear Physics Grants DE-FG02-97ER41041 and DE-FG02-97ER41033. I would like to acknowledge the staff of the UNC Chapel Hill and TUNL machine shops, and experimental collaborators A. Adekola, G. Rusev, S. Stave, M.W. Ahmed and Y. Wu for their help in completing these experiments.

-
- [1] J. K. Sprinkle Jr., H. O. Menlove, M. C. Miller, and P. A. Russo, Los Alamos National Lab Report No. LA-12496-MS, 11 (1993).
 - [2] H. R. Weller, M. W. Ahmed, H. Gao, W. Tornow, Y. K. Wu, M. Gai, and R. Miskimen, Prog. Part. Nucl. Phys., **62**, 257 (2009).
 - [3] A. K. Thompson, “Source activity,” (2009), private communication.
 - [4] R. C. Martin, J. B. Knauer, and P. A. Balo, Oak Ridge National Laboratory Report (1999).
 - [5] A. B. Smith, P. R. Fields, and J. H. Roberts, Phys. Rev., **108**, 411 (1957).
 - [6] C. A. Burke, M. T. Lunnon, and H. W. Lefevre, Phys. Rev. C, **10**, 1299 (1974).
 - [7] C. A. Burke, Ph.D. thesis, University of Oregon (1972).
 - [8] J. H. Gibbons and R. L. Macklin, Phys. Rev., **114**, 571 (1959).
 - [9] K. K. Sekharan, H. Laumer, B. D. Kern, and F. Gabbard, Nuc. Instr. and Meth., **133**, 253 (1976).
 - [10] V. N. Litvinenko *et al.*, Phys. Rev. Lett., **78**, 4569 (1997).
 - [11] C. Sun, Y. Wu, G. Rusev, and A. Tonchev, Nuc. Instr. Meth. Phys A, **605**, 312 (2009).
 - [12] C. Sun, Ph.D. thesis, Duke University (2009).
 - [13] R. Schiavilla, Phys. Rev. C, **72**, 034001 (2005).
 - [14] Y. Birenbaum, S. Kahane, and R. Moreh, Phys. Rev. C, **32**, 1825 (1985).
 - [15] R. Moreh, T. J. Kennett, and W. V. Prestwich, Phys. Rev. C, **39**, 1247 (1989).
 - [16] A. De Graeve, R. Van de Vyver, A. Zieger, C. Van den Abeele, L. Van Hoorebeke, D. Ryckbosch, H. Ferdinande, F. De Smet, B. Ziegler, P. Wilhelm, and H. Arenhövel, Phys. Rev. C, **45**, 860 (1992).
 - [17] K. Y. Hara, H. Utsunomiya, S. Goko, H. Akimune, T. Yamagata, M. Ohta, H. Toyokawa, K. Kudo, A. Uritani, Y. Shibata, Y.-W. Lui, and H. Ohgaki, Phys. Rev. D, **68**, 072001

429 (2003).

430 [18] J. H. Hubbell and S. M. Seltzer, NIST Standard Reference Database 126 (1989).

431 [19] M. Chadwick *et al.*, Nuclear Data Sheets, **107**, 2931 (2006), evaluated Nuclear Data File
432 ENDF/B-VII.0.

433 [20] MCNPX *User's Manual* (2007).